

1 **Multi-point Observation of Hiss Emerging from Lightning Whistlers**

2 **O. Santolík^{1,2}, I. Kolmašová^{1,2}, J. S. Pickett³, D. A. Gurnett³**

3 ¹ Department of Space Physics, Institute of Atmospheric Physics of the Czech Academy of
4 Sciences, Prague, Czechia.

5 ² Faculty of Mathematics and Physics, Charles University, Prague, Czechia.

6 ³ Department of Physics and Astronomy, University of Iowa, Iowa City, Iowa, USA.

7

8 Corresponding author: Ondrej Santolík (os@ufa.cas.cz)

9

10 **Key Points:**

- 11 • We use multi-point measurements of electromagnetic field fluctuations by the Cluster
12 spacefleet to discuss the origin of plasmaspheric hiss.
- 13 • Our case study shows hiss which was triggered in the dayside outer plasmasphere by
14 unducted whistlers emitted from strong lightning strokes.
- 15 • Spectral properties of magnetospherically reflecting whistlers and hiss strongly depend
16 on geographical location of the source thunderstorm.

17

18 **Abstract**

19 We analyze continuous multi-point measurements of electromagnetic field waveforms onboard
20 the Cluster spacecraft in order to contribute to the discussion on sources of plasmaspheric hiss,
21 known as a shaping agent for the Earth radiation belts. In our case study we aim at finding
22 sources of hiss observed close to the geomagnetic equator in the outer plasmasphere on the
23 dayside. We find hiss to be triggered from whistlers of different spectral properties. Whistlers
24 with the lowest observed dispersion arrive to different spacecraft with time delays indicating
25 their origin in the northern hemisphere. Positions of source lightning discharges are then found
26 using the time coincidences with the Word Wide Lightning Location Network data from three
27 active thunderstorm regions in Europe. We find that subionospheric propagation of lightning
28 atmospheric is necessary to explain the observations. Geographic locations of their ionospheric
29 exit points then determine spectral properties of resulting unducted whistlers and triggered hiss.
30 We conclude that magnetospherically reflecting whistlers are a good candidate for one of the
31 embryonic sources of plasmaspheric hiss.

32

33 **1 Introduction**

34 Plasmaspheric hiss occurs in high plasma density regions surrounding the Earth as band-limited
35 whistler mode waves (Russell et al., 1969; Dunckel and Helliwell, 1969; Thorne et al., 1973)
36 with a well-defined intensity maximum at frequencies near a few hundred herz and on the
37 dayside (Spasojevic et al., 2015; Li et al., 2015; Meredith et al., 2018).

38 These waves strongly influence the dynamics of the radiation belts (Van Allen, 1959),
39 causing pitch angle diffusion and subsequent losses of electrons to the atmosphere (Kennel and
40 Petschek, 1966), especially from the slot region between the inner and outer radiation belts
41 (Lyons et al., 1972). These effects are highly variable (Watt et al., 2019, Zhu et al., 2021) and
42 organized by the position of the plasmopause (Malaspina et al., 2020). Hiss acts together with
43 other wave emissions also in the outer radiation belt (Drozdov et al., 2020), occurring at larger
44 radial distances in plasmaspheric drainage plumes (Zhang et al., 2019).

45 The origin of plasmaspheric hiss is still under debate. Thorne et al. (1973, 1979), and
46 Church and Thorne (1983) originally proposed a mechanism of the in situ growth and

47 amplification starting from background electromagnetic turbulence or from an embryonic source.
48 This is, at least in some cases, supported by in situ observations of the amplification rate
49 (Solomon et al., 1988) or by observations of hiss propagating to both hemispheres from the
50 equatorial region close to the plasmapause (Parrot and Lefeuvre, 1986, Santolík et al., 2001) or
51 in plasmaspheric plumes (Laakso et al., 2015). Other cases when hiss propagated close to the
52 whistler mode resonance cone in the equatorial region are not easily reconcilable with this
53 hypothesis (Storey et al., 1991).

54 Church and Thorne (1983) proposed three possibilities for the embryonic source of
55 plasmaspheric hiss:

- 56 1. Chorus emissions (Storey, 1953) entering the plasmasphere at high latitude;
- 57 2. The low-frequency component of ducted whistlers that originate in lightning activity
58 (Storey, 1953);
- 59 3. Auroral hiss (Gurnett and O'Brien, 1964) entering near the ionospheric foot of the
60 plasmasphere and propagating into the plasmasphere via the magnetospherically
61 reflected whistler mode.

62 The first suggestion has been verified by ray tracing studies of Chum and Santolík
63 (2005), and Santolík et al. (2006), proving that chorus can enter the plasmasphere and provide an
64 embryonic source of plasmaspheric hiss. Bortnik et al. (2007, 2008, 2009, 2011) confirmed this
65 scenario and suggested that plasmaspheric hiss might be generally explained by accumulation of
66 chorus which propagates into the plasmasphere and evolves into hiss without local amplification.
67 However, Hartley et al. (2019) found that chorus wave vectors are rarely favorable for accessing
68 the plasmasphere and evolving into hiss and that chorus most probably doesn't directly
69 contribute to a significant fraction of plasmaspheric hiss.

70 Concerning the second suggestion of Church and Thorne (1983) for the embryonic source
71 of plasmaspheric hiss, Sonwalker and Inan (1989) reported that magnetospherically reflected
72 whistlers (Kimura, 1966; Smith and Angerami, 1968; Edgar, 1976) often trigger hiss emissions
73 and therefore serve as an embryonic source. Draganov et al. (1993) put forward a hypothesis that
74 simple accumulation of many nonducted whistlers can explain the presence of hiss in the
75 plasmasphere. Green et al. (2005) showed that longitudinal, seasonal, and local time distribution

76 of the hiss intensity is similar to the distribution of lightning, with a conclusion that lightning is
77 the dominant source for plasmaspheric hiss. In the follow-up discussion, Meredith et al. (2006)
78 concluded that there is no relation between whistlers and hiss under 2 kHz on the global scale.
79 However, results of Green et al. (2005) have been recently supported by Záhlava et al. (2019).
80 Furthermore, importance of whistlers for the precipitation of energetic electrons in the radiation
81 belts has been stressed by Bortnik et al. (2003) and Rodger et al. (2003). Green et al. (2020) also
82 showed a significant contribution of whistlers at frequencies below 2 kHz.

83 Santolík and Chum (2009), commenting on conclusions of Bortnik et al. (2009),
84 suggested that at different times plasmaspheric hiss may arise by different mechanisms, while
85 none of them can explain all the obtained observations. To contribute to this discussion, we have
86 reexamined the mechanism of Sonwalker and Inan (1989), using the multi-point data recorded by
87 the WBD instruments on Cluster 1, 3 and 4 spacecraft during the close separation campaign on
88 4th July 2013, when all three Cluster spacecraft recorded the same sequence of lightning
89 generated whistlers which induced hiss bands. Section 2 is devoted to the description of our data
90 set, Section 3 shows results of a detailed analysis of the observed whistlers, and Section 4
91 describes their source lightning discharges. The results are discussed in Section 5, and Section 6
92 contains brief conclusions of our study.

93

94 **2 Data**

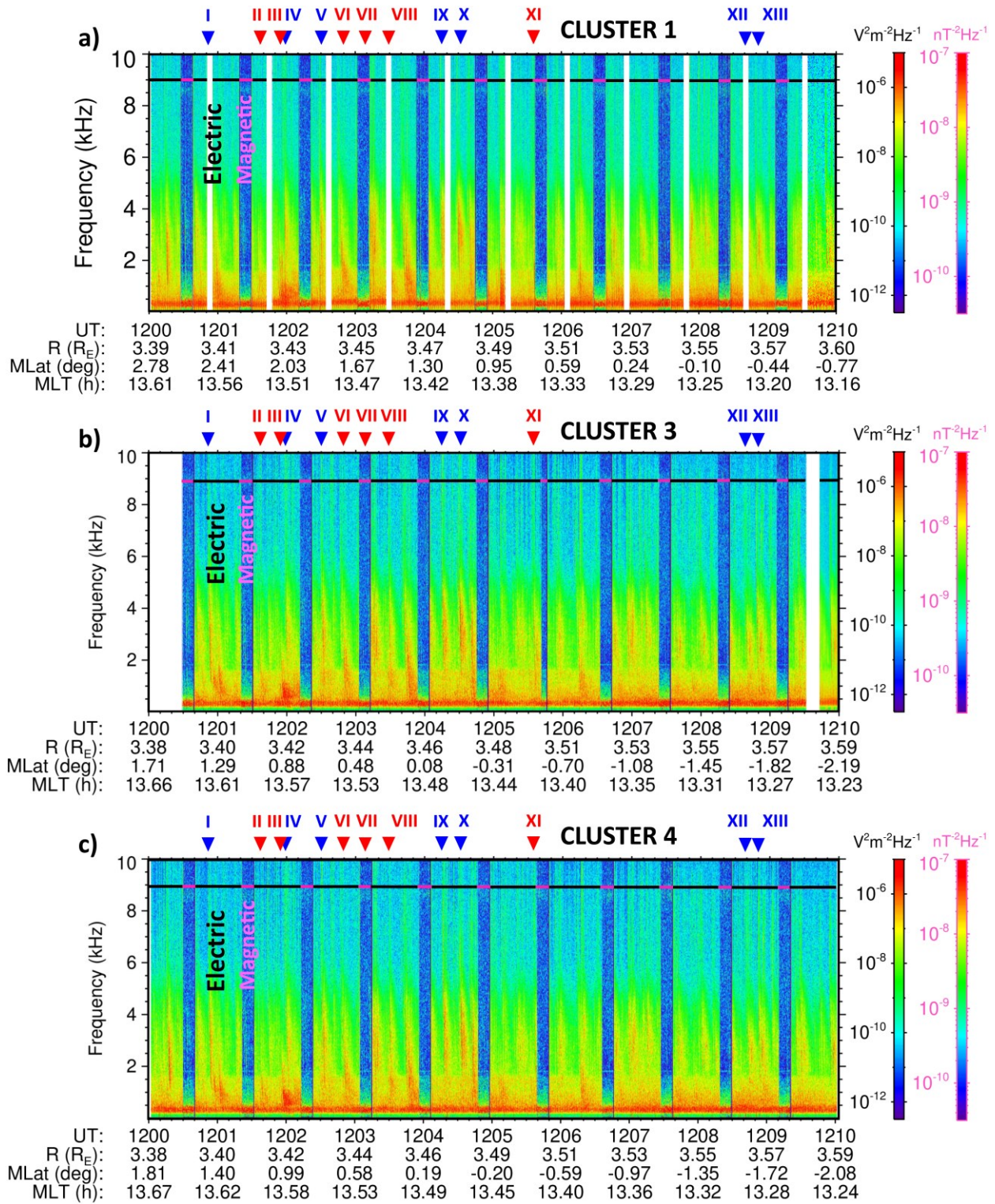
95 The present study is based on the Wide Band Data (WBD) instruments onboard the Cluster
96 spacefleet (Gurnett et al., 1997, 2001), which primarily provide us with multi-point
97 measurements of fluctuations of the electric field detected by one of the 88 m long double probe
98 electric field antennas (Gustafsson et al., 1997) with effective lengths of 52-53 m (Béghin et al.,
99 2005). The input of the WBD instruments can be alternatively switched to the signals from one
100 of the search coil sensors (Cornilleau-Wehrin et al., 1997).

101 Direct telemetry transmissions of real time data from the WBD instruments were received
102 by the NASA Deep Space Network (DSN) stations before October 2007, when two 10m dishes
103 of the Panska Ves telemetry station (operated by the Institute of Atmospheric Physics of the
104 Czech Academy of Sciences) have been added to the telemetry receiving network. Starting

105 January 2015, only Panska Ves station receives the real time WBD telemetry. Another downlink
106 possibility is to record data at a decreased rate into the onboard memory during the burst mode
107 operations, and channel them eventually to the ESA ground stations together with the telemetry
108 of other Cluster instruments.

109 During the analyzed interval on the 4th of July 2013 between 12:00 and 12:10 UT,
110 Cluster 3 and 4 were approximately 40 km apart and the separation of this pair from Cluster 1
111 was approximately 500 km. The WBD instruments on Cluster 3 and 4 were switched to a mode,
112 in which the measurements are continuously recorded with a sampling frequency of 27.4 kHz
113 and 8 bits per sample, in a pass band between 25 Hz and 9.5 kHz. Electric field antennas E_y and
114 E_z , which are located in the spin plane, were respectively used on Cluster 3 and 4 as sensors,
115 replaced on each spacecraft by the magnetic search coil antenna B_x during the transmission
116 intervals of the active sounder (Décréau et al., 1997). In these cases, the search coil
117 characteristics limit the bandwidth below 4 kHz.

118 As Cluster 3 and Cluster 4 were at close separations, the real time telemetry streams from
119 both spacecraft were received by a single dish Y (PAN80) of the Panska Ves station. The
120 telemetry of Cluster 1 was acquired through the burst mode operations with the onboard storage,
121 resulting in a data rate reduced to one third of the original value. The records are thus not
122 continuous but form a cycle of ~40 milliseconds long data intervals followed always by ~80 ms
123 long gaps. The data structure is otherwise the same as on Cluster 4, with alternating E_z and B_x
124 components.



125

126 **Figure 1.** Frequency-time spectrograms obtained from waveform measurements of (a) Cluster 1,
 127 (b) Cluster 3, and (c) Cluster 4 on the 4th of July 2013 between 12:00 and 12:10 UT. Electric
 128 and magnetic field measurements are interleaved, as shown by the color coded black-magenta

129 *horizontal line on the top of each spectrogram. Representative alternating blocks of electric and*
130 *magnetic data are indicated near the start of the spectrogram with bold black and magenta*
131 *colored text, respectively. Magnetic field power spectral densities are given in $nT^2 Hz^{-1}$, with the*
132 *corresponding color scales on the right hand side of each spectrogram, while electric field*
133 *power spectral densities in $V^2 m^{-2} Hz^{-1}$ are coded according to the second color scale from the*
134 *right. Thirteen selected intervals of 10 seconds (according to Table 1) are marked by roman*
135 *numerals I - XIII on the top of each panel. Blue and red numerals respectively denote the type 1*
136 *and type 2 whistlers, examples of which are given in Fig. 2. Positions of each spacecraft are*
137 *given on the bottom of the corresponding panels: radial distance R in the Earth radii, magnetic*
138 *latitude $Mlat$ in degrees, and magnetic local time MLT in hours.*

139

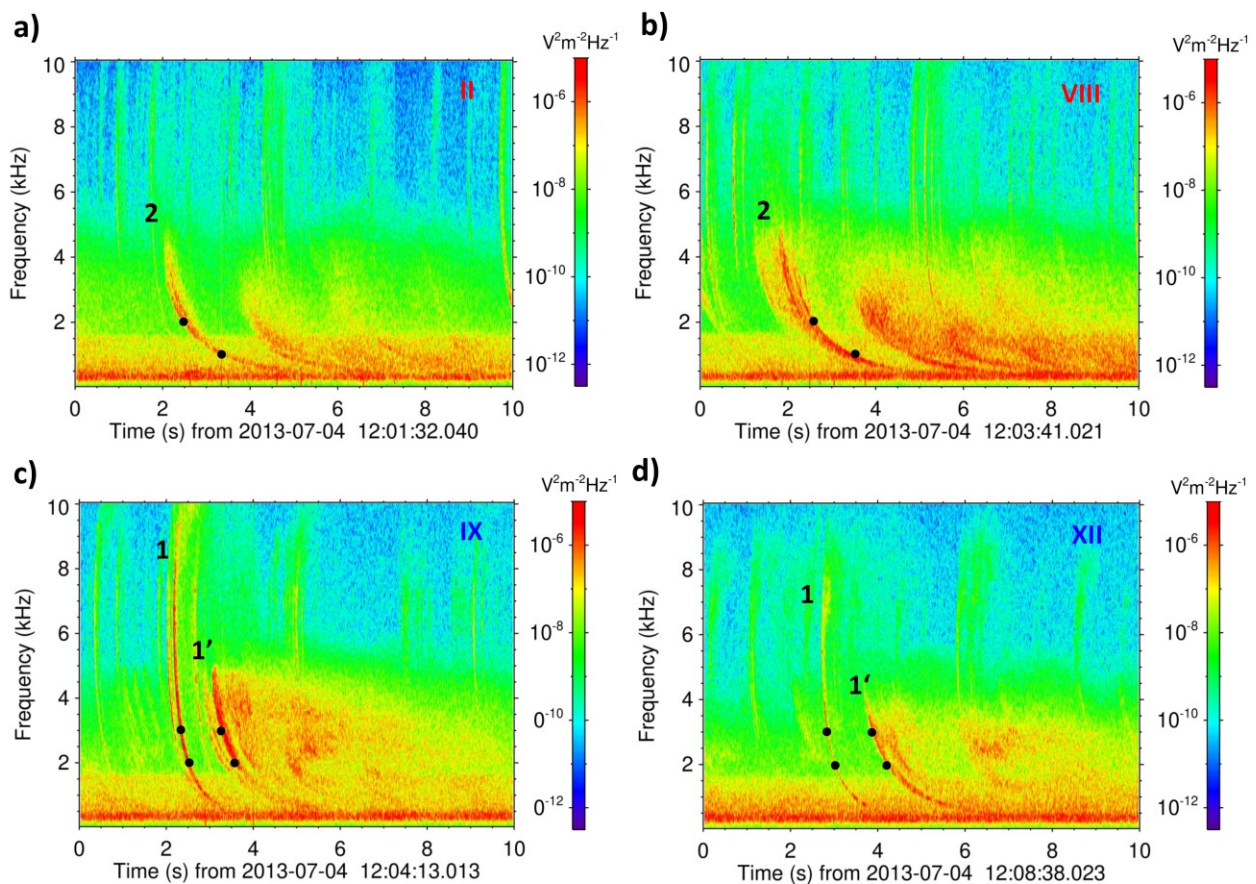
140 An overview of the data set is shown in Fig. 1. Cluster 3, 4, and 1 move one after the
141 other along roughly the same orbit, crossing successively the magnetic equator from the northern
142 to the southern hemisphere. The measurements were recorded on the dayside, at a radial distance
143 of 3.5 Earth radii. All three spacecraft are still in the plasmasphere with high plasma densities
144 above $80 cm^{-3}$, exceeding the upper limit of the active sounder and consistent with a very small
145 potential difference of the probes at the tips of electric antennas relative to the spacecraft body
146 (not shown). The WBD observations are very similar on the three closely separated spacecraft.
147 The measurement cycle with a duration of 52 s repeats approximately synchronously on the three
148 spacecraft, alternating $\sim 10s$ long magnetic field measurements with the electric field
149 measurements in the remaining part of the cycle. On the time scale of 10 minutes, shown in
150 Fig. 1, we can identify several distinct features. (i) A steady hiss band at few hundreds of Hz is
151 detected by electric and magnetic antennas. (ii) Electric antennas detect a weaker and also
152 relatively stable hiss band with an upper frequency cutoff around 1.5 kHz, with a weak
153 counterpart in the magnetic field measurements. (iii) Frequent bursts of broadband hiss detected
154 at the same time by the different spacecraft at frequencies up to 4-5 kHz are also found mainly in
155 the electric field measurements.

156

157 **3 Whistlers**

158 A closer look at the data on the time scales of several seconds reveals that hiss is accompanied
 159 by whistlers which originate from return strokes of lightning discharges in the Earth's
 160 atmosphere (Storey, 1953). Whistlers occur throughout the entire analyzed interval. Many of
 161 them are overlapping and from those which occur separately we have selected thirteen intervals
 162 of 10 s which are marked by roman numerals I - XIII in Fig. 1.

163



164

165 **Figure 2.** Examples of four selected 10 s intervals, which are respectively marked by II, VIII, IX
 166 and XII in the overview Figure 1. (a,b) Type 2 whistlers from intervals II and VIII; (c,d) type 1
 167 whistlers from intervals IX and XII. In all cases, electric field power spectral density is obtained
 168 from spectral analysis of waveform data recorded by Cluster 3 by using a 512 point FFT with
 169 50% overlapping and averages over 5 neighboring spectra. Black dots show time delays and
 170 frequencies that we use to calculate whistler dispersions for three types of traces: 1, 1' and 2.

171

172 We have found two distinct patterns in the recorded whistlers which we denote as type 1
173 and type 2 whistlers. Examples are given in Fig. 2, where we show power spectral densities
174 obtained from electric field waveforms recorded by Cluster 3 during intervals II, VIII, IX, and
175 XII. Other spacecraft provide us with very similar spectrograms from these intervals. We can see
176 that the latter two intervals in Fig. 2c and 2d contain a distinct whistler trace 1 with a lower
177 dispersion and with a nose frequency (Helliwell et al., 1956; Helliwell, 1965) around 6 kHz,
178 which is, as expected, slightly higher than one quarter of the local electron cyclotron frequency
179 ($f_{ce} = 18.8$ kHz) obtained from magnetic field measurements onboard the Cluster 3 spacecraft.

180 Trace 1 is followed by a blurred higher dispersion trace 1', which is accompanied by
181 weaker hiss at frequencies above 2 kHz, sometimes showing also signs of subsequent whistler
182 traces, especially for strong whistlers. These patterns often repeat in our data set as "type 1"
183 whistlers, occurring 7 times in our selected set of 13 intervals. Intervals in figures 2a and 2b
184 show blurred whistler traces triggering intense bursts of hiss below 2-3 kHz and followed, for
185 strong whistlers, by one or more traces with higher dispersion. These "type 2" intervals repeat 6
186 times in the selected set occasionally preceded with a very weak trace with a low dispersion,
187 similar to type 1 trace.

Inter- val no.	Whist- ler trace type	start time UT (hour: min)	start time UT (s)	t_1 from start time (s)	f_1 (kHz)	t_2 from start time (s)	f_2 (kHz)	D (sv/Hz)	t_0 from start time (s)	Estimated UT of the causative lightning		WWLLN World Wide Lightning Location Network Corresponding strokes			
										(hours : min)	(s)	Universal Time	Lat (°N)	Lon (°E)	Peak current (kA)
I	1	12:00	48.019	2.231	3.5	2.365	2.5	43.27	1.500	12:00	49.519	12:00:49.326314	59.22	38.29	147
	1'	12:00	48.019	3.867	2	4.200	1.5	96.26							
II	2	12:01	32.040	2.437	2	3.268	1	89.72	0.431	12:01	32.471	12:01:32.150764	47.55	28.33	96
	2	12:01	50.019	2.762	2	3.663	1	97.28	0.587	12:01	50.606	12:01:50.441402	45.63	32.36	163
IV	1	12:01	50.019	7.794	4	8.046	2	38.48	7.186	12:01	57.205	12:01:56.891150	57.57	38.59	180
	1'	12:01	50.019	8.983	3	9.355	2	90.66							
V	1	12:02	29.037	0.259	4	0.399	3	57.24	-0.646	12:02	28.391	12:02:28.607433	59.45	38.86	135
	1'	12:02	29.037	1.468	3	1.860	2	95.53							
VI	2	12:02	46.020	1.719	2	2.560	1	90.80	-0.311	12:02	45.709	12:02:45.418684	45.13	32.57	213
	2	12:03	03.000	2.073	2	2.919	1	91.32	0.031	12:03	3.031	none			
VIII	2	12:03	41.021	3.630	2	4.525	1	96.63	2.469	12:03	41.490	12:03:41.125780	48.25	26.16	293
	1	12:04	13.013	2.310	3	2.511	2	48.99	2.416	12:04	14.429	none			
IX	1'	12:04	13.013	3.324	3	3.680	2	86.76							
	1	12:04	27.008	3.009	3	3.184	2	42.65	3.230	12:04	29.240	12:04:28.979911	59.23	38.34	236
X	1'	12:04	27.008	4.089	3	4.466	2	91.88							
	2	12:05	34.000	1.136	2	1.987	1	91.85	-0.918	12:05	34.082	12:05:34.062749	44.54	33.67	60
XII	1	12:08	38.023	2.861	3	3.036	2	42.65	2.082	12:08	40.105	none			
	1'	12:08	38.023	3.890	3	4.227	2	82.13							
XIII	1	12:08	49.025	1.210	3.5	1.267	3	42.09	0.499	12:08	49.524	12:08:49.138110	57.45	38.52	247
	1'	12:08	49.025	2.253	3	2.610	2	87.00							

188

189

Table 1. Results of analysis of 13 selected whistler intervals, see text for details

190 We estimated the dispersion coefficients D for all these whistler traces using the classical
 191 method based on the cold plasma approach (Stix, 1992) in a quasi-parallel approximation for a
 192 dense plasma at frequencies well below the nose frequency,

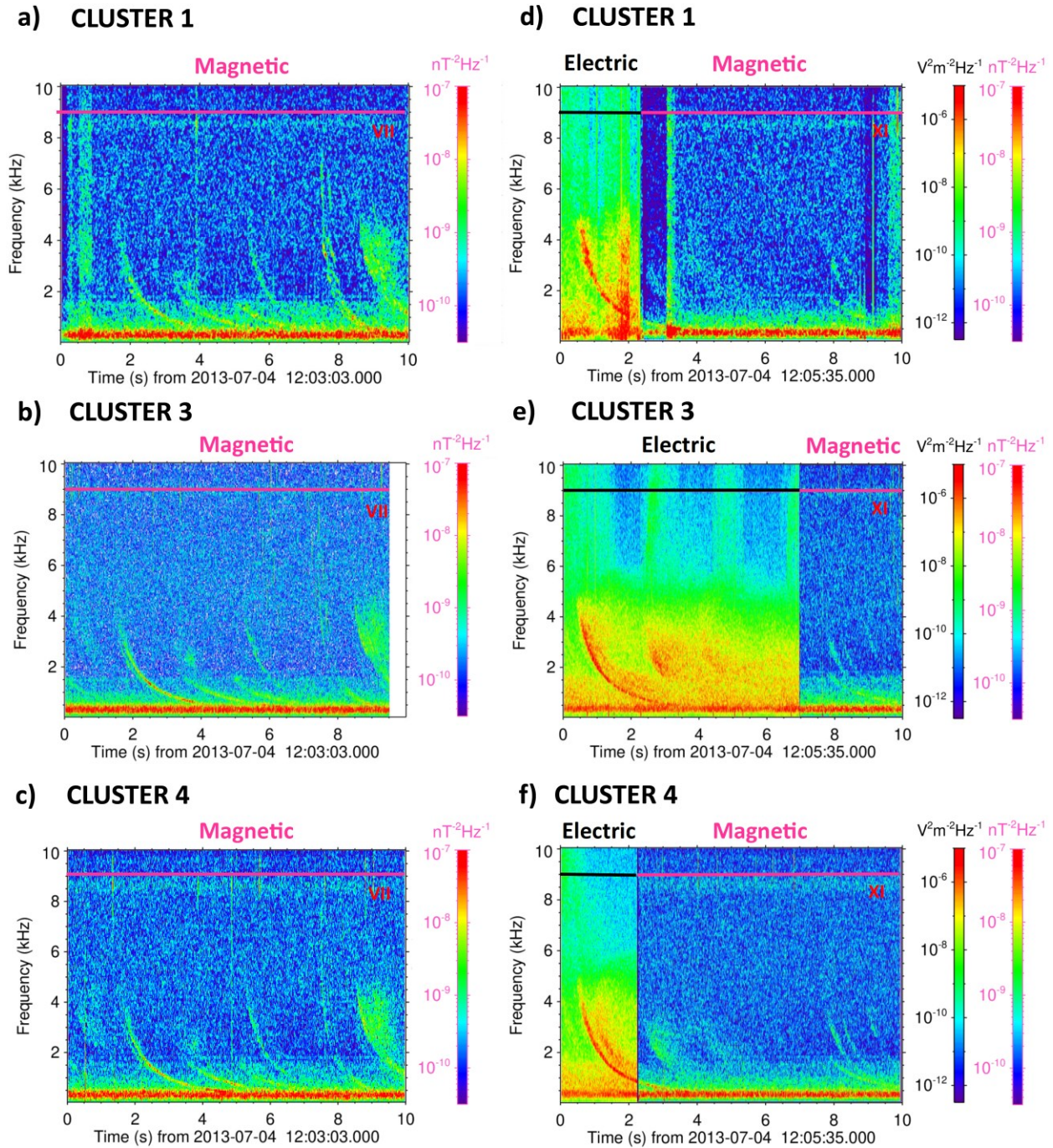
$$201 \quad t = t_0 + \frac{D}{\sqrt{f}}, \quad (1)$$

193 where t is the time of arrival of the whistler trace at a selected frequency f from an originally
 194 broadband source emitting at time t_0 . We chose frequencies f_1 and f_2 so that the whistler trace
 195 can be accurately scanned from the frequency-time spectrograms, and we determined the
 196 corresponding times t_1 and t_2 . A typical uncertainty of the estimated frequency is around 5 Hz
 197 and a typical uncertainty of time estimation ranges from 50 ms (for trace 1) to 100 ms (for traces
 198 1' or 2). This analysis allows us to estimate the dispersion coefficients D and source times t_0 for
 199 all the analyzed whistler traces 1, 1', and 2. The results, based on Cluster 3 data from the 13
 200 selected intervals, are summarized in Table 1.

202 The average dispersion coefficient from all trace 1 results is $D_1 = 45 \pm 7$ s $\sqrt{\text{Hz}}$, while the
 203 average dispersion coefficient from the trace 1' analysis was $D_{1'} = 90 \pm 5$ s $\sqrt{\text{Hz}}$. Analysis of type
 204 2 whistler traces yields a very similar average dispersion coefficient, $D_2 = 93 \pm 3$ s $\sqrt{\text{Hz}}$. This
 205 strongly suggests a similar mechanism for the 1' and 2 traces. The simplest possible explanation
 206 therefore is that the whistler trace 1 corresponds to a half-hop whistler propagating to the equator
 207 from the source lightning directly to the spacecraft, without any reflections. Whistler traces 1'
 208 and 2 would then correspond to whistlers after the first magnetospheric reflection, where for
 209 type 2 events the rays of the original half-hop whistlers miss the spacecraft position.

210

211



212

213 **Figure 3.** Frequency-time spectrograms obtained from the magnetic field waveforms recorded
 214 during interval VII by (a) Cluster 1, (b) Cluster 3, and (c) Cluster 4. Spectrograms from the same
 215 three spacecraft for interval XI when the electric field measurements have been switched to the
 216 magnetic field at a different time on (e) Cluster 3 than on (d) Cluster 1 and (f) Cluster 4.

217

218 To verify this hypothesis on propagation of whistlers and to estimate possible effects of
 219 associated hiss it is important to know if the waves are electromagnetic or if some of the
 220 observed features correspond to quasi-electrostatic waves. Fig. 3 shows data for the intervals
 221 where signals of the magnetic search coil antennas were used as the WBD input on the three
 222 spacecraft. Frequency-time spectrograms from interval VII in Fig 3a-c clearly show the magnetic
 223 field components of type 2 whistler traces (with a corresponding dispersion coefficient of
 224 $91 \text{ s}\sqrt{\text{Hz}}$, see Table 1) converging into an intense hiss band at hundreds of hertz, and
 225 accompanied by faint signatures of the hiss band with the upper cutoff around 1.5 kHz. Hiss
 226 bursts following the whistler traces at frequencies above 2 kHz are also observed.

227 Spectrograms from interval XI shown in Fig. 3d-f provide us with the opportunity to
 228 compare the electric and magnetic components of the measured waves, as the WBD input on
 229 Cluster 3 was switched to the magnetic antenna later than on the two other spacecraft.
 230 Comparison of power spectral densities of the electric field and magnetic field for hiss at a
 231 frequency $f \sim 300 \text{ Hz}$ results in a ratio of magnetic to electric field amplitudes $cB / E \sim 50$,
 232 where c is the speed of light. This is roughly consistent with the expected value, obtained as

$$242 \quad cB / E = \frac{f_{pe}}{\sqrt{f(f_{ce} - f)}} \quad (2)$$

233 assuming quasiparallel propagating whistler mode waves in a cold plasma (Stix, 1992) with a
 234 density of $\sim 200 \text{ cm}^{-3}$ and the corresponding plasma frequency f_{pe} , yielding $cB / E \sim 54$ with
 235 the measured electron cyclotron frequency $f_{ce} = 18.8 \text{ kHz}$. Onboard analysis of measurements
 236 by the triaxial search coil sensors (Cornilleau-Wehrin et al., 1997), averaged over 4 s
 237 measurement intervals, indeed indicates a right handed polarization of hiss at 300 Hz. This
 238 confirms the presence of whistler mode waves and excludes the presence of the X-mode
 239 equatorial noise below the lower hybrid frequency ($f_{lh} \sim 470 \text{ Hz}$). However, the measured
 240 magnetic field fluctuations are not well confined to a single plane so any further propagation
 241 analysis is not possible using this data set (not shown).

243 The observed type 2 whistler trace, with a dispersion coefficient of $92 \text{ s}\sqrt{\text{Hz}}$ (see Table 1)
 244 is partly seen in both the electric and magnetic field data but the ratio of magnetic to electric field
 245 amplitudes is substantially lower than for the 300 Hz hiss, with $cB / E \sim 20\text{-}30$, indicating
 246 propagation at large angles between the wave vector and the background magnetic field line. The

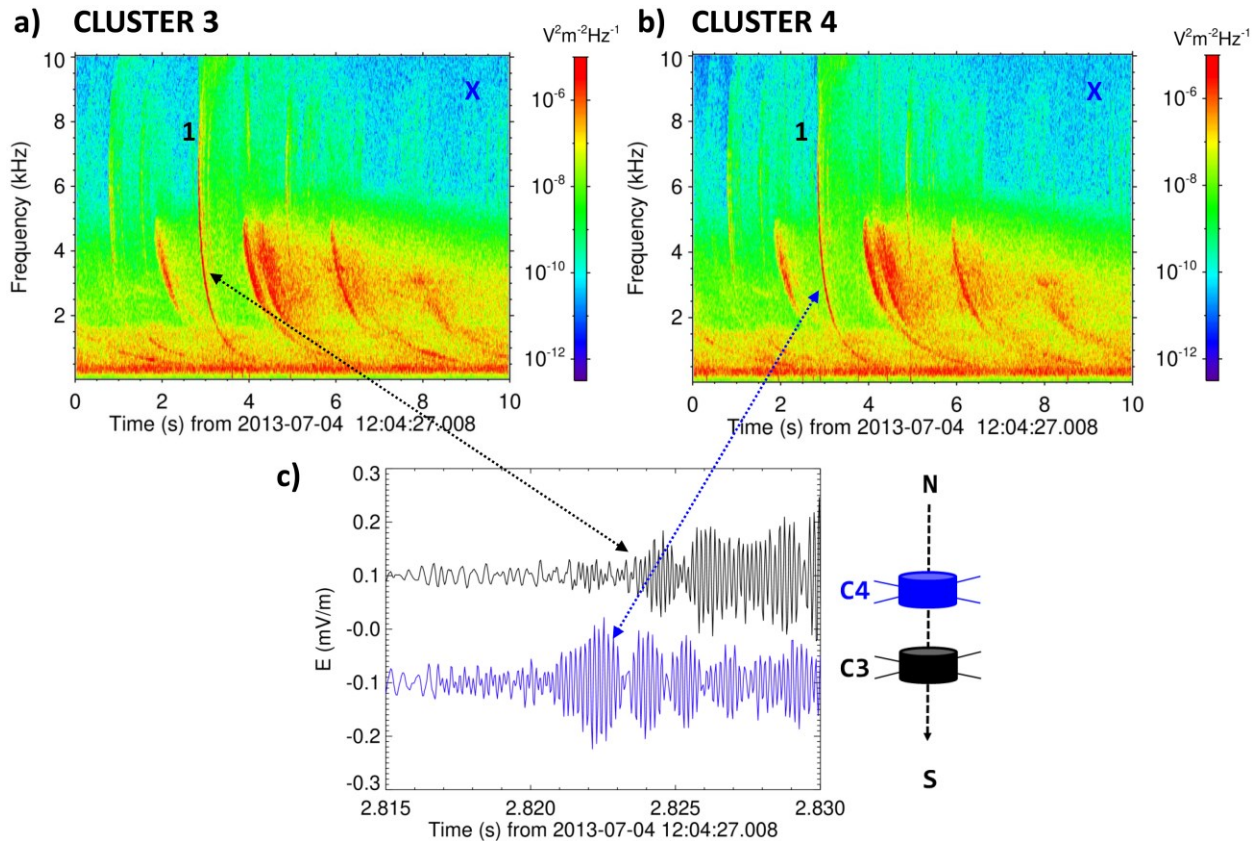
247 same holds true for the following reflection and induced hiss at above 2 kHz. Hiss below 1.5 kHz
 248 shows even lower values of $cB / E \sim 15$, which indicates propagation closer to the whistler mode
 249 resonance angle.

250 Unfortunately, this comparison is not available for the type 1 whistlers in our data set.
 251 Therefore, a question still remains: why do we observe two separate types of lightning whistlers,
 252 some of which are clearly able to contribute to hiss both below and above 2 kHz? We start
 253 answering this question by analyzing multi-spacecraft measurements. We can benefit from the
 254 close separation of Cluster spacecraft and analyze the time of arrival of the nose of the sharp
 255 whistler trace 1. A rough calculation of the group velocity based on the cold plasma
 256 approximation (Stix, 1992) for quasi-parallel propagation in a dense plasma,

$$257 \quad v_g = \frac{2c}{f_{pe}f_{ce}} (f_{ce} - f)^{3/2} f^{1/2} \quad (3)$$

258 yields an expected minimum time delay of one millisecond between Cluster 3 and Cluster 4 at
 259 the nose frequency $f = 6$ kHz, for plasma densities above 100 cm^{-3} . Realistically higher plasma
 260 densities and oblique propagation only increase this time delay, and it therefore can be detected
 261 using the WBD waveform measurements.

262



263

264 **Figure 4.** (a,b) Electric field power spectral density, which were respectively obtained from
 265 spectral analysis of waveform data recorded by Cluster 3 and Cluster 4 during interval X. (c)
 266 Initial part of the electric field waveforms of the type 1 whistler trace, shown by a black line for
 267 Cluster 3 and by a blue line for Cluster 4.

268

269 Figure 4 shows a type 1 whistler from interval X. Power spectrograms from Cluster 3 and
 270 Cluster 4 in Figs 4a and 4b give nearly identical pictures with a sharp first whistler trace, but
 271 detailed electric field waveform recordings from both spacecraft in Fig. 4c clearly show
 272 differences in the initial part of the whistler signature. Both spacecraft detect arrival of strongly
 273 modulated sinusoidal signals of the first intensification, with approximately 6 wave periods per
 274 millisecond, corresponding well to the estimated nose frequency of 6 kHz. The subsequent
 275 amplitude modulation can be explained by beating of coherent monochromatic waves above and
 276 below the nose frequency, which arrive later. The time of arrival of the first signal is, as
 277 expected, different by a few ms on the two spacecraft, Cluster 4 detecting it first. As Cluster 4 is
 278 to the North from Cluster 3, it is clear that the whistlers arrive from the northern hemisphere.

279 This propagation pattern is observed for all first traces in the analyzed intervals of type 1
280 whistlers.

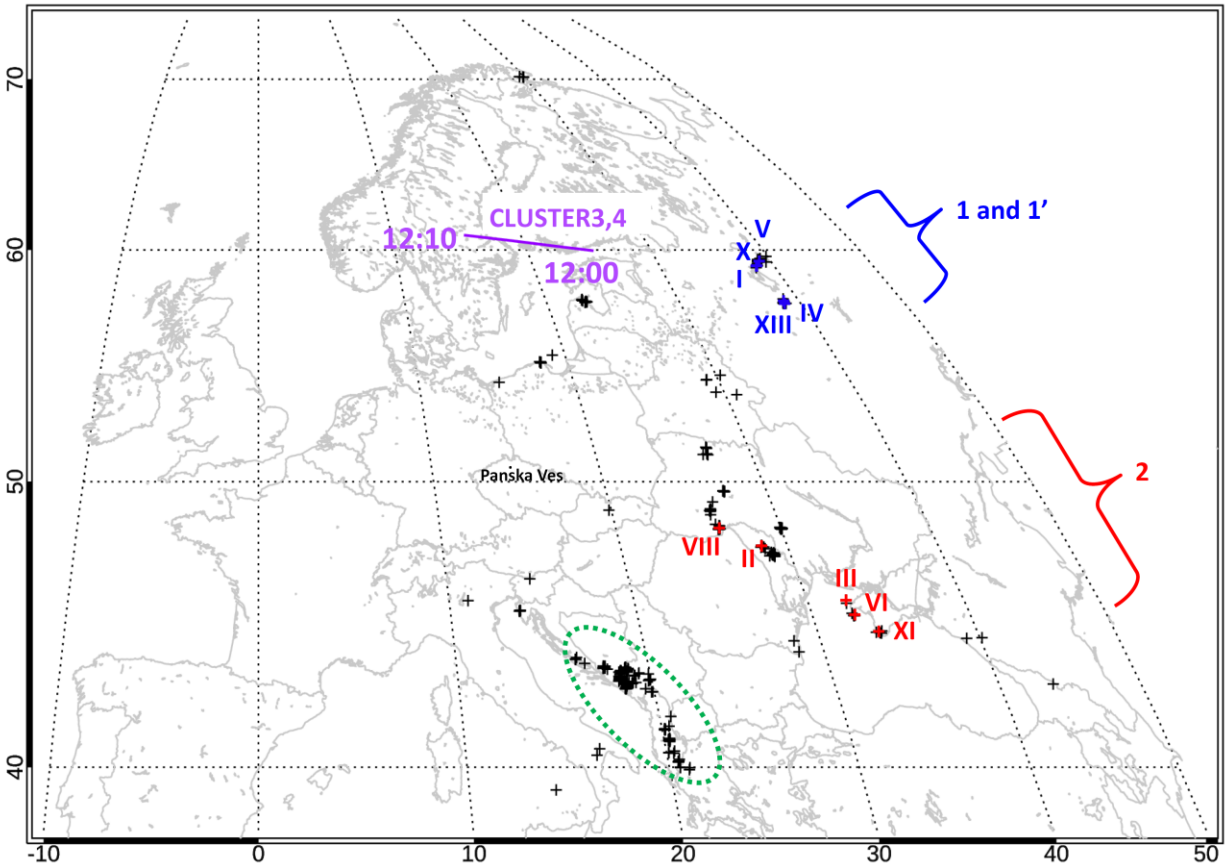
281

282 **4 Source lightning**

283 Assuming that type 1 whistler traces arrive directly from their sources as half-hop whistlers we
284 can identify their source lightning return strokes using the data of one of the ground based
285 lightning location networks. We used the data of the World Wide Lightning Location Network
286 (WWLLNN), which are obtained using time of arrival analysis of signals from very low
287 frequency sensors distributed at 70 different locations around the globe. Their detection
288 efficiency depends on location, time of the day, and strength of the stroke (Hutchins et al.,
289 2012a) but for strong lightning with peak currents larger than 50 kA the absolute efficiency was
290 evaluated to be around 75% over New Zealand (Holzworth et al., 2019).

291 Over Europe, where the Cluster 3 and Cluster 4 spacecraft have their magnetic footprints
292 during the analyzed parts of their orbits (see the purple line in Fig. 5, linked to the real time
293 reception in Panska Ves), the density of the WWLLN detectors is high and we can therefore
294 expect that we would be able to find sources for the majority of whistlers originating in strong
295 discharges. The strength of the discharges was measured by the WWLLN stroke energy, which
296 we converted to the more usual peak current estimator using relations derived by Hutchins et al.
297 (2012b).

298



299

300 **Figure 5.** Map of WLLN lightning locations (shown as black '+' signs) over Europe on 4 July
 301 2013 between 12:00 and 12:10 UT. The magnetic footprints of the Cluster 3 and Cluster 4 orbits
 302 (purple line) are nearly identical. Identified source strokes for type 1 and type 2 whistlers are
 303 respectively shown in blue and red, annotated by the roman numerals corresponding to the
 304 analyzed intervals. Strokes from an Adriatic storm at lower latitudes are encircled by a green
 305 dotted line.

306

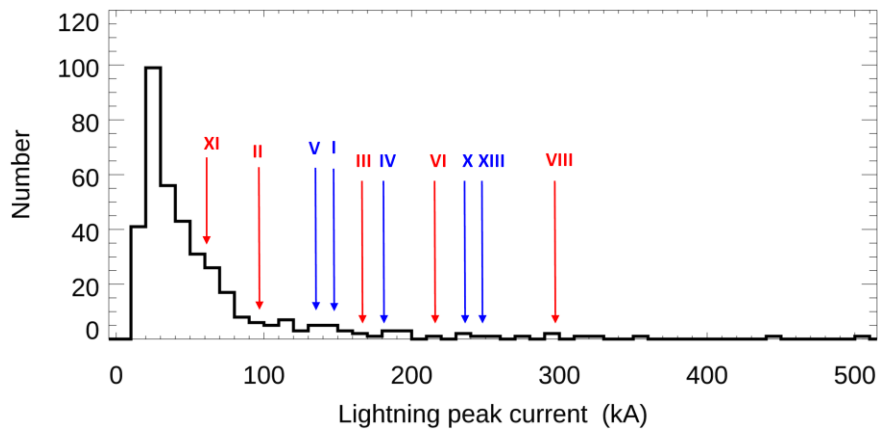
307 Black '+' signs in Fig. 5 show all WLLN stroke locations in the geographic region at
 308 latitudes above 30°N and longitudes between 10°W and 50°E, obtained on the 4th of July 2013
 309 between 12:00 and 12:10 UT. From this set of 377 individual lightning strokes we have selected
 310 those, which have their WLLN stroke time within 400 ms from the time t_0 obtained from the
 311 Cluster 3 data using equation (1). Out of the analyzed 13 whistler intervals, for 3 we didn't find
 312 any corresponding WLLN stroke, for 2 we found a single corresponding stroke, for 6 we

313 found two candidate strokes, for 1 we found three strokes, and for the remaining one four
 314 strokes.

315 In these cases, where we obtained two or more possible strokes fulfilling our criterion, all
 316 but one corresponded to multiple strokes from the same lightning flash at the same location. We
 317 have then selected the strongest stroke, which always was the first one in the sequence. Table 1
 318 summarizes the positions and equivalent peak currents of these estimated source strokes. Their
 319 positions are plotted in Fig. 5 which clearly shows that the causative lightning return strokes for
 320 type 1 whistlers are found closer to the magnetic footprint of the spacecraft, at higher geographic
 321 latitudes of 57.5° - 59.5° N, corresponding to 53.0° - 54.8° of the geomagnetic dipole latitude. The
 322 causative lightning return strokes of type 2 whistlers are found at lower latitudes of 44.5° - 48.3° N
 323 (41.1° - 45.9° of the geomagnetic dipole latitude). We also found an intense thunderstorm activity
 324 in the Adriatic region between 40° and 43.5° N (38.9° - 43° of the geomagnetic dipole latitude).

325

326



327

328 **Figure 6.** Histogram of WWLLN equivalent peak currents obtained from 377 lightning strokes
 329 shown as black '+' signs in Fig. 5. Arrows with roman numerals show the peak currents of
 330 identified source strokes for the type 1 (blue) and type 2 (red) whistlers.

331

332 Noting that the sources are displaced from the spacecraft magnetic footprint, we expect
 333 that only strong lightning strokes can feed sufficient electromagnetic energy into the Earth-
 334 ionosphere waveguide, so that the resulting atmospherics can travel to a distant exit point and
 335 generate the observed whistlers. Relation of the equivalent peak current of the identified source

336 strokes for the type 1 and type 2 whistlers to the overall distribution of peak currents in the
337 analyzed geographical region and time interval is given in Fig. 6. The results confirm that the
338 whistler source lightning strokes tend to be placed on the tail of the distribution at high peak
339 currents, with no clear differences of the source peak currents for the two types of whistlers.

340

341 **5 Discussion**

342 Although source lightning discharges of the type 2 whistlers are located at larger distances from
343 the spacecraft magnetic footprint (1400 to 1900 km) compared to sources of the type 1 whistlers
344 (800 and 1300 km), they do not tend to be generated by stronger lightning. At the same time, the
345 spectral forms of the two types of whistlers are different. A plausible explanation of both these
346 observations is as follows:

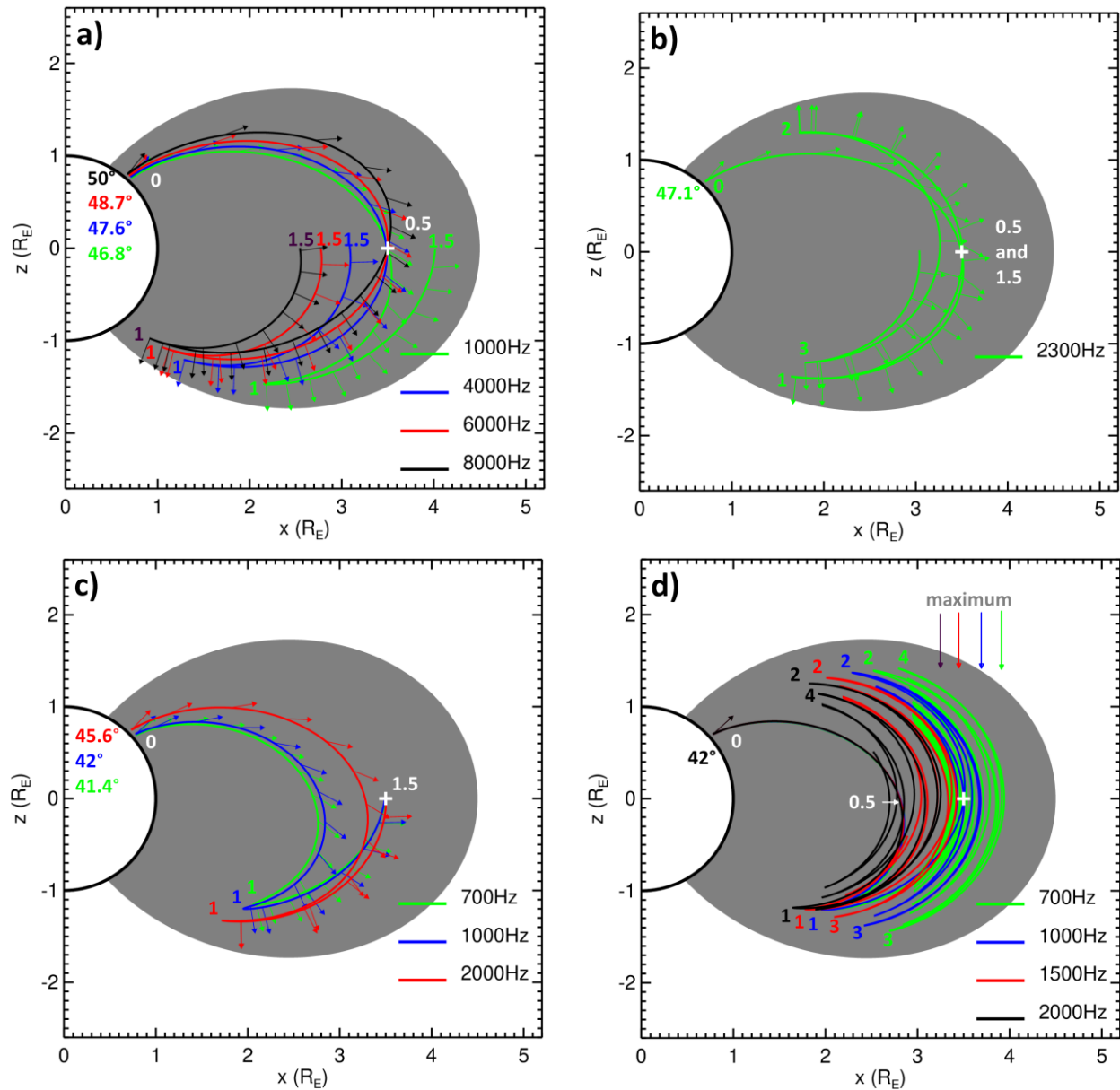
- 347 (i) the lightning discharges generate atmospherics with a broadband frequency spectrum
348 which propagate in the Earth-ionosphere waveguide to all horizontal directions
349 radially from their source;
- 350 (ii) part of their electromagnetic power continuously leaks into the ionosphere during this
351 subionospheric propagation;
- 352 (iii) the leaked power quickly decreases with the distance of the ionospheric exit point
353 from the source lightning discharge but the measurable affected area has a radius of at
354 least 2000 km around a strong lightning (Fišer et al., 2010; Burkholder et al., 2013);
- 355 (iv) the Snell's law implies wave vector directions which are very close to the local
356 vertical direction at the exit points, determining thus boundary conditions for their
357 subsequent propagation into the magnetosphere;
- 358 (v) the waves propagate in an unducted mode (Kimura, 1966; Smith and Angerami,
359 1968; Edgar, 1976; Shklyar and Jiříček, 2000; Santolík et al., 2009) upward from
360 their exit points, each frequency along a slightly different path;
- 361 (vi) the type 1 whistler traces observed by the spacecraft correspond to the half-hop
362 propagation from the ionosphere to the equator - the whistlers are then composed of
363 different frequencies from the same source, each of them arriving from a slightly

- 364 different ionospheric exit point at higher latitudes, which the atmospheric from the
365 type 1 source lightning discharges reach with acceptably low attenuation;
- 366 (vii) another set of ionospheric exit points corresponds to separate frequencies of type 1'
367 or type 2 whistlers which are observed after the first magnetospheric reflection: lower
368 frequencies observed in type 2 case would also correspond to lower latitudes of the
369 corresponding ionospheric exit points;
- 370 (viii) hiss bands are triggered by these whistlers (Sonwalker and Inan, 1989), but also by
371 whistlers reflecting many times in the magnetosphere (Bortnik et al., 2003) where
372 discharges at yet lower latitudes of the Adriatic storm might contribute to an
373 embryonic source of hiss below 1.5 kHz.

374 To verify if these scenarios are realistic for both types of whistlers we performed a
375 schematic ray-tracing simulation, based on the procedure of Cerisier (1970) with a diffusive
376 equilibrium model of the plasma density distribution, modified to include an adaptive integration
377 step by Santolík et al. (2006, 2009). The model in our case was set to an exospheric temperature
378 of 700K and calibrated to a plasma density of 10^4 cm^{-3} at a reference altitude of 700km. This
379 model is necessarily only a crude approximation of the real plasma density distribution in the
380 magnetosphere but it is sufficient to demonstrate the properties of wave propagation, which lead
381 to the observed effects.

382 Figure 7a shows that only a relatively narrow interval of 3.2° for ionospheric exit points
383 at higher latitudes is needed to account for an unducted half-hop propagation of different
384 frequency components to a spacecraft located at the magnetic equator at a radial distance of 3.5
385 Earth radii. The waves arrive with wave vectors that are obliquely inclined from the focal
386 magnetic field line by $58\text{-}60^\circ$, which is still sufficiently far from the whistler mode resonance
387 cone to account for the electromagnetic nature of these waves. These rays would correspond to
388 the half-hop (trace 1) part of type 1 whistlers whose source discharges have been detected at
389 higher latitudes. Following the rays past the spacecraft we may notice them undergoing a
390 magnetospheric reflection and returning to the equator at different places far from the spacecraft:
391 low frequencies, represented by the ray at 1 kHz return to larger radial distances, and high
392 frequencies (4, 6, and 8 kHz) return to lower radial distances than the spacecraft position.

393



394

395

396 **Figure 7.** Schematic ray tracing simulation from the ionosphere to the Cluster spacecraft shown
 397 by a white '+' sign at the equator and at a radial distance of 3.5 Earth radii. The plot is drawn
 398 in the plane of the local magnetic meridian containing the spacecraft position in Cartesian
 399 coordinates x - z where z is parallel to the magnetic dipole axis. (a) Type 1 whistler trace for
 400 color coded frequencies 1-8 kHz (b) Ray for a frequency of 2.3 kHz (c) Type 2 whistler trace for
 401 color coded frequencies 0.7-2 kHz (d) Rays exiting from the geomagnetic dipole latitude of 42°
 402 trace for color coded frequencies 0.7-2 kHz during 10s of the group time, with their maximum
 403 radial distances shown on the top. Geomagnetic dipole latitudes of the ionospheric exit points of
 404 the separate rays are given on the left hand side of each panel. Exit points are marked by white

405 “0”, equatorial passes are marked by “0.5” and “1.5”, magnetospheric reflections are
406 identified by color coded numbers 1, 2, 3, and 4. Arrows are added to the rays to show the wave
407 vector directions with an interval of 100 ms of the group time. Grey area follows the magnetic
408 field line passing through the equator at a radial distance of 4.5 Earth radii.

409

410 A frequency between 1 and 4 kHz must therefore exist, for which the corresponding ray
411 passes through the spacecraft not only as a half-hop whistler but also after the magnetospheric
412 reflection. Fig. 7b show such a ray for a frequency of 2.3 kHz, which would then contribute to
413 both type 1 and type 1' traces. Further evolution of the ray during first three magnetospheric
414 reflections indicates that the waves gradually move to lower radial distances.

415 Fig. 7c corresponds to possible propagation of type 2 whistlers. Waves at frequencies
416 below 2.3 kHz, all of them launched from lower latitudes than in the previous case, initially miss
417 the spacecraft position and converge at the spacecraft location only after the first magnetospheric
418 reflection. Their wave vector directions at that point are inclined by 77-79° from the local field
419 line. This is still far enough (5-11°) from the resonance cone, which explains the observed
420 electromagnetic nature of these waves. Occasional very weak half-hop whistlers preceding the
421 type 2 traces could be explained by a long propagation and strong attenuation of the lightning
422 generated atmospherics in the Earth-ionosphere waveguide.

423 Finally, a long lasting hiss emission below 1.5 kHz might be, at least in part, attributed to
424 embryonal sources from whistlers originating in the Adriatic storm at geomagnetic latitudes
425 below 43°. Unducted whistlers can bounce in the magnetosphere back and forth with many
426 reflections. Bortnik et al. (2003) showed that the lifetime of these waves is limited by the wave
427 damping caused by the low energy component of the electron distribution function. At the
428 equatorial distance of 3.5 Earth radii, their results give lifetimes of at least 20 s, which accounts
429 for many reflections. Fig. 7d shows rays propagating for 10 s from an exit point at a geomagnetic
430 latitude of 42°, from which the 2 kHz waves always stay at lower radial distances and do not
431 reach the spacecraft but waves below 1.5 kHz propagate to larger radial distances up to the
432 spacecraft position.

433

434 **6 Conclusions**

435 Detailed analysis of high cadence multi-point measurements of electromagnetic field by
436 the Cluster spacefleet allowed us to reconstruct the chain of events leading to the occurrence of
437 triggered hiss in the outer edge of the equatorial dayside plasmasphere. Sources of triggering
438 waves for these emissions are found in lightning discharges localized by the Word Wide
439 Lightning Location Network to different thunderstorms spread over 15° of geomagnetic latitude.
440 The location of the source lighting determines the spectral shapes and frequencies of the
441 resulting unducted whistlers. Our case study demonstrates that lightning whistlers penetrating the
442 ionosphere at latitudes around 40° of geomagnetic latitude and propagating unducted should be
443 considered as one of the embryonic sources of plasmaspheric hiss below 2 kHz.

444

445 **Acknowledgments and Data Availability**

446 We thank our colleagues at the Panská Ves station (Jakub Horký, Jiří Šimůnek, Michal Siman,
447 and Jiří Baše) for their tireless work on receptions of the Cluster WBD direct telemetry. We are
448 especially grateful for the work of the late Jan Šmilauer who was at the beginning of this effort.
449 The work on the present paper has received funding from the European Union's Horizon 2020
450 research and innovation programme under grant agreement No. 870437 (SafeSpace), from the
451 GAČR grant No. 20-09671S, and from the European Regional Development Fund-Project
452 CRREAT (CZ.02.1.01/0.0/0.0/15_003/0000481). The data supporting the conclusions of this
453 paper can be obtained from the European Space Agency's Cluster Science Archive on
454 <https://www.cosmos.esa.int/web/csa>

455

456 **References**

- 457 Béghin, C., Décréau, P. M. E., Pickett, J., Sundkvist, D. & Lefebvre, B. (2005). Modeling of
458 Cluster's electric antennas in space: Application to plasma diagnostics. *Radio Sci.*, *40*,
459 RS6008. doi:10.1029/2005RS003264
- 460 Bortnik, J., Inan, U. S., & Bell, T. F. (2003). Energy distribution and lifetime of
461 magnetospherically reflecting whistlers in the plasmasphere. *J. Geophys. Res.*, *108*, 1199.
462 doi:10.1029/2002JA009316

- 463 Bortnik, J., Thorne, R. M., Meredith, N. P., & Santolík, O. (2007). Ray tracing of penetrating
 464 chorus and its implications for the radiation belts. *Geophys. Res. Lett.*, *34*, L15109.
 465 doi:10.1029/2007GL030040
- 466 Bortnik, J., Thorne, R. M., & Meredith, N. P. (2008). The unexpected origin of plasmaspheric
 467 hiss from discrete chorus emissions. *Nature*, *452*(7183), 62–66. doi: 10.1038/nature06741
- 468 Bortnik, J., Li, W., Thorne, R. M., Angelopoulos, V., Cully, C., Bonnell, J., Le Contel, O., &
 469 Roux, A. (2009). An observation linking the origin of plasmaspheric hiss to discrete chorus
 470 emissions. *Science*, *324* (5928), 775–778. doi:10.1126/science.1171273
- 471 Bortnik, J., L. Chen, Li, W., Thorne, R. M., & Horne, R. B. (2011). Modeling the evolution of
 472 chorus waves into plasmaspheric hiss. *J. Geophys. Res.*, *116*, A08221.
 473 doi:10.1029/2011JA016499
- 474 Burkholder, B. S., Hutchins, M. L., McCarthy, M. P., Pfaff, R. F. & Holzworth, R. H. (2013).
 475 Attenuation of lightning-produced sferics in the Earth-ionosphere waveguide and low-latitude
 476 ionosphere. *J. Geophys. Res. Space Physics*, *118*, 3692–3699. doi:10.1002/jgra.50351
- 477 Cerisier, J. (1970). Propagation perpendiculaire au voisinage de la fréquence de la résonance
 478 hybride basse, in *Plasma Waves in Space and in the Laboratory*, vol. 2, pp. 487–521,
 479 Edinburgh Univ. Press, Edinburgh, U. K.
- 480 Chum, J., & Santolík, O. (2005). Propagation of whistler-mode chorus to low altitudes: divergent
 481 ray trajectories and ground accessibility. *Ann. Geophys.*, *23*, 3727–3738. doi:10.5194/angeo-
 482 23-3727-2005
- 483 Church, S. R., & Thorne, R. M. (1983). On the origin of plasmaspheric hiss: Ray path integrated
 484 amplification. *J. Geophys. Res.*, *88* (A10), 7941– 7957. doi:10.1029/JA088iA10p07941
- 485 Cornilleau-Wehrin, N., Chauveau, P., Louis, S. et al. (1997). The Cluster Spatio-Temporal
 486 Analysis of Field Fluctuations (STAFF) Experiment. *Space Science Reviews* *79*, 107–136.
 487 doi:10.1023/A:1004979209565
- 488 Décréau, P. M. E., et al. (1997). WHISPER, a resonance sounder and wave analyser:
 489 Performances and perspectives for the Cluster mission. *Space Sci. Rev.*, *79*, 157–193.
 490 doi:10.1023/A:1004931326404
- 491 Draganov, A. B., Inan, U. S., Sonwalkar, V. S., & Bell, T. F. (1993). Whistlers and
 492 plasmaspheric hiss: Wave directions and three-dimensional propagation. *J. Geophys. Res.*,
 493 *98*(A7), 11401– 11410. doi:10.1029/93JA00662

- 494 Drozdov, A. Y., Usanova, M. E., Hudson, M. K., Allison, H. J., & Shprits, Y. Y. (2020). The
495 role of hiss, chorus, and EMIC waves in the modeling of the dynamics of the multi-MeV
496 radiation belt electrons. *Journal of Geophysical Research: Space Physics*, *125*,
497 e2020JA028282. doi:10.1029/2020JA028282
- 498 Dunckel, N., & Helliwell, R. A. (1969). Whistler-mode emissions on the OGO 1 satellite. *J.*
499 *Geophys. Res.*, *74*(26), 6371–6385. doi:10.1029/JA074i026p06371
- 500 Edgar, B. C. (1976). The upper- and lower-frequency cutoffs of magnetospherically reflected
501 whistlers. *J. Geophys. Res.*, *81*(1), 205–211. doi:10.1029/JA081i001p00205
- 502 Fišer, J., Chum, J., Diendorfer, G., Parrot, M., & Santolík, O. (2010). Whistler intensities above
503 thunderstorms. *Ann. Geophys.* *28*, 37–46. doi:10.5194/angeo-28-37-2010
- 504 Green, J. L., Boardsen, S., Garcia, L., Taylor, W. W. L., Fung, S. F. & Reinisch, B. W. (2005).
505 On the origin of whistler mode radiation in the plasmasphere. *J. Geophys. Res.*, *110*, A03201.
506 doi:10.1029/2004JA010495
- 507 Green, A., Li, W., Ma, Q., Shen, X.-C., Bortnik, J., & Hospodarsky, G. B. (2020). Properties of
508 lightning generated whistlers based on Van Allen Probes observations and their global effects
509 on radiation belt electron loss. *Geophysical Research Letters*, *47*, e2020GL089584.
510 doi:10.1029/2020GL089584
- 511 Gurnett, D. A., & O'Brien, B. J. (1964). High-latitude geophysical studies with satellite Injun 3:
512 5. Very-low-frequency electromagnetic radiation. *J. Geophys. Res.*, *69*(1), 65–89.
513 doi:10.1029/JZ069i001p00065
- 514 Gurnett, D. A., Huff, R. L., & D. L. Kirchner (1997). The wide-band plasma wave investigation.
515 *Space Sci. Rev.*, *79*, 195–208. doi:10.1023/A:1004966823678
- 516 Gurnett, D. A., Huff, R. L., Pickett, J. S., Persoon, A. M., Mutel, R. L. et al. (2001). First results
517 from the Cluster wideband plasma wave investigation. *Annales Geophysicae* *19*, 1259-1272.
- 518 Gustafsson, G. et al. (1997). The electric field and wave experiment for the Cluster mission.
519 *Space Sci. Rev.*, *79*, 137–156. doi:10.1023/A:1004975108657
- 520 Hartley, D. P., Kletzing, C. A., Chen, L., Horne, R. B., & Santolík, O. (2019). Van Allen Probes
521 observations of chorus wave vector orientations: Implications for the chorus-to-hiss
522 mechanism. *Geophysical Research Letters*, *46*, 2337-2346. doi:10.1029/2019GL082111
- 523 Helliwell, R. A., Crary, J. H., Pope, J. H., & Smith, R. L. (1956). The “nose” whistler—A new
524 high-latitude phenomenon. *J. Geophys. Res.*, *61*(1), 139–142. doi:10.1029/JZ061i001p00139

- 525 Helliwell, R. (1965). Whistlers and Related Ionospheric Phenomena. Stanford University Press,
526 Stanford, California.
- 527 Holzworth, R. H., McCarthy, M. P., Brundell, J. B., Jacobson, A. R., & Rodger, C. J. (2019).
528 Global distribution of superbolts. *Journal of Geophysical Research: Atmospheres*, *124*, 9996–
529 10,005. doi:10.1029/2019JD030975
- 530 Hutchins, M. L., Holzworth, R. H., Brundell, J. B. & Rodger, C. J. (2012a). Relative detection
531 efficiency of the World Wide Lightning Location Network. *Radio Sci.*, *47*, RS6005.
532 doi:10.1029/2012RS005049
- 533 Hutchins, M. L., R. H. Holzworth, C. J. Rodger, and J. B. Brundell (2012b). Far-field power of
534 lightning strokes as measured by the World Wide Lightning Location Network. *J. Atmos.*
535 *Oceanic Technol.*, *29*, 1102–1110. doi:10.1175/JTECH-D-11-00174.1
- 536 Kennel, C. F., & Petschek, H. E. (1966). Limit on stably trapped particle fluxes. *J. Geophys.*
537 *Res.*, *71*(1), 1–28. doi:10.1029/JZ071i001p00001
- 538 Kimura, I. (1966). Effects of Ions on Whistler-Mode Ray Tracing. *Radio Science*, *1*, 269-283.
539 doi: 10.1002/rds196613269
- 540 Laakso, H., Santolík, O., Horne, R., Kolmašová, I., Escoubet, P., Masson, A. & Taylor, M.
541 (2015). Identifying the source region of plasmaspheric hiss. *Geophys. Res. Lett.*, *42*, 3141-
542 3149. doi:10.1002/2015GL063755
- 543 Li, W., Ma, Q., Thorne, R. M., Bortnik, J., Kletzing, C. A., Kurth, W. S., Hospodarsky, G. B. &
544 Nishimura, Y. (2015). Statistical properties of plasmaspheric hiss derived from Van Allen
545 Probes data and their effects on radiation belt electron dynamics. *J. Geophys. Res. Space*
546 *Physics*, *120*, 3393–3405. doi:10.1002/ 2015JA021048
- 547 Lyons, L. R., Thorne, R. M., & Kennel, C. F. (1972). Pitch-angle diffusion of radiation belt
548 electrons within the plasmasphere. *J. Geophys. Res.*, *77* (19), 3455–3474.
549 doi:10.1029/JA077i019p03455
- 550 Malaspina, D. M., Zhu, H., & Drozdov, A. Y. (2020). A wave model and diffusion coefficients
551 for plasmaspheric hiss parameterized by plasmopause location. *Journal of Geophysical*
552 *Research: Space Physics*, *125*, e2019JA027415. doi:10.1029/2019JA027415
- 553 Meredith, N. P., Horne, R. B., Clilverd, M. A., Horsfall, D., Thorne, R. M. & Anderson, R. R.
554 (2006). Origins of plasmaspheric hiss. *J. Geophys. Res.* *111*, A09217.
555 doi:10.1029/2006JA011707

- 556 Meredith, N. P., Horne, R. B., Kersten, T., Li, W., Bortnik, J., Sicard, A., & Yearby, K. H.
557 (2018). Global model of plasmaspheric hiss from multiple satellite observations. *Journal of*
558 *Geophysical Research: Space Physics*, *123*, 4526–4541. doi:10.1029/2018JA025226
- 559 Parrot, M., & Lefeuvre, F. (1986). Statistical study of the propagation characteristics of ELF hiss
560 observed on GEOS-1, inside and outside the plasmasphere. *Ann. Geophys*, *4*, 363
- 561 Rodger, C. J., Clilverd, M. A., & McCormick, R. J. (2003). Significance of lightning-generated
562 whistlers to inner radiation belt electron lifetimes. *J. Geophys. Res.*, *108*, 1462.
563 doi:10.1029/2003JA009906
- 564 Russell, C. T., Holzer, R. E., & Smith, E. J. (1969). OGO 3 observations of ELF noise in the
565 magnetosphere: 1. Spatial extent and frequency of occurrence. *J. Geophys. Res.*, *74*(3), 755–
566 777. doi:10.1029/JA074i003p00755
- 567 Santolík, O., Parrot, M., Storey, L. R. O., Pickett, J. S., & Gurnett, D. A. (2001). Propagation
568 analysis of plasmaspheric hiss using Polar PWI measurements. *Geophys. Res. Lett.* *28*(6),
569 1127-1130. doi:10.1029/2000GL012239
- 570 Santolík, O., Chum, J., Parrot, M., Gurnett, D. A., Pickett, J. S., & Cornilleau-Wehrin, N.
571 (2006). Propagation of whistler mode chorus to low altitudes: Spacecraft observations of
572 structured ELF hiss. *J. Geophys. Res.*, *111*, A10208. doi:10.1029/2005JA011462
- 573 Santolík, O. & Chum, J. (2009). The origin of plasmaspheric hiss. *Science* *324*, 729 – 730. doi:
574 10.1126/science.1172878, 2009
- 575 Santolík, O., Parrot, M., Inan, U. S., Burešová, D., Gurnett, D. A., & Chum, J. (2009).
576 Propagation of unducted whistlers from their source lightning: A case study. *Journal of*
577 *Geophysical Research*, *114*, A03212. doi:10.1029/2008JA013776
- 578 Shklyar, D. R. & Jiříček, F. (2000). Simulation of nonducted whistler spectrograms observed
579 aboard the MAGION 4 and 5 satellites. *Journal of Atmospheric and Solar-Terrestrial Physics*
580 *62*(5), 347-370. doi: 10.1016/S1364-6826(99)00097-8
- 581 Smith, R. L., & Angerami, J. J. (1968). Magnetospheric properties deduced from OGO 1
582 observations of ducted and nonducted whistlers. *J. Geophys. Res.*, *73*(1), 1–20.
583 doi:10.1029/JA073i001p00001
- 584 Solomon, J., Cornilleau-Wehrin, N., Korth, A., & Kremser, G. (1988). An experimental study of
585 ELF/VLF hiss generation in the Earth's magnetosphere. *J. Geophys. Res.*, *93*(A3), 1839–1847.
586 doi:10.1029/JA093iA03p01839

- 587 Sonwalkar, V. S., & Inan, U. S. (1989). Lightning as an embryonic source of VLF hiss. *J.*
588 *Geophys. Res.*, *94*(A6), 6986–6994. doi:10.1029/JA094iA06p06986
- 589 Spasojevic, M., Shprits, Y. Y., & Orlova, K. (2015). Global empirical models of plasmaspheric
590 hiss using Van Allen Probes. *Journal of Geophysical Research: Space Physics*, *120*(12),
591 10370–10383. doi:10.1002/2015JA021803
- 592 Stix, T. H. (1992). *Waves in Plasmas*, Springer, New York, ISBN 978-0-88318-859-0.
- 593 Storey L. R. O. (1953). An investigation of whistling atmospherics. *Philosophical Transactions*
594 *of the Royal Society of London. Series A, Mathematical and Physical Sciences* *246*, 113–141.
595 doi:10.1098/rsta.1953.0011
- 596 Storey, L. R. O., Lefeuvre, F., Parrot, M., Cairó, L., & Anderson, R. R. (1991). Initial survey of
597 the wave distribution functions for plasmaspheric hiss observed by ISEE 1. *J. Geophys. Res.*,
598 *96*(A11), 19469–19489. doi:10.1029/91JA01828
- 599 Thorne, R. M., Smith, E. J., Burton, R. K., & Holzer, R. E. (1973). Plasmaspheric hiss. *Journal*
600 *of Geophysical Research: Space Physics*, *78*(10), 1581–1596. doi:10.1029/JA078i010p01581
- 601 Thorne, R., Church, S., & Gorney, D. (1979) On the origin of plasmaspheric hiss: The
602 importance of wave propagation and the plasmopause. *J. Geophys. Res.*, *84*(A9), 5241–5247.
603 doi:10.1029/JA084iA09p05241
- 604 Van Allen, J. A. (1959). The geomagnetically trapped corpuscular radiation. *J. Geophys. Res.*,
605 *64*(11), 1683–1689. doi:10.1029/JZ064i011p01683
- 606 Watt, C. E. J., Allison, H. J., Meredith, N. P., Thompson, R. L., Bentley, S. N., Rae, I. J., et al.
607 (2019). Variability of quasilinear diffusion coefficients for plasmaspheric hiss. *Journal of*
608 *Geophysical Research: Space Physics*, *124*. doi:10.1029/2018JA026401
- 609 Záhlava, J., Nemeč, F., Santolík, O., Kolmašová, I., Hospodarsky, G. B., Parrot, M., et al.
610 (2019). Lightning contribution to overall whistler mode wave intensities in the plasmasphere.
611 *Geophysical Research Letters*, *46*, 8607–8616. doi:10.1029/2019GL083918
- 612 Zhang, W., Ni, B., Huang, H., Summers, D., Fu, S., Xiang, Z., et al. (2019). Statistical properties
613 of hiss in plasmaspheric plumes and associated scattering losses of radiation belt electrons.
614 *Geophysical Research Letters*, *46*, 5670–5680. doi:10.1029/2018GL081863
- 615 Zhu, Q., Cao, X., Gu, X., Ni, B., Xiang, Z., Fu, S., et al. (2021). Empirical loss timescales of slot
616 region electrons due to plasmaspheric hiss based on Van Allen Probes observations. *Journal*
617 *of Geophysical Research: Space Physics*, *126*, e2020JA029057. doi:10.1029/2020JA029057